Draft version July 24, 2025
Typeset using LaTeX default style in AASTeX631

Asteroseismic Models of the Magnetic Binary HD 156424

Serena Davis,[1] C.C. Lovekin,[1] and V. Khalack[2]

[1] *Mount Allison University, 67 York St. Sackville, NB, Canada*
[2] *Université de Moncton Moncton, NB, Canada*

ABSTRACT

HD 156424 is a hot magnetic star in the Sco OB4 association, and has previously been identified as part of a binary system. Spectropolarimetric results show that the companion star is also strongly magnetic, and thus this is a rare example of a doubly magnetic hot binary. In this work, we present a more detailed analysis of TESS data, including phase variation. We find short term phase variation consistent with an oblique magnetic rotator, as well as long term phase variation consistent with the third element proposed by Shultz et al. (2021). We performed asteroseismic modelling of the star, and determined the pulsations are most likely associated with the primary of the system. Our best fit models are universally young, and we find the star is well fit by a model with M=9.8 $M_\odot$.

1. INTRODUCTION

Magnetic fields have been detected in about 10% of OB stars (Mathis & Bugnet 2023). OB stars lack the surface convection zone responsible for generating the magnetic field in low-mass stars, and the existing magnetic fields are thought to be fossil in origin. Nevertheless, many OB stars have been discovered to have strong ($>$ 1 kG) magnetic fields. This includes both HD 156424A and its companion Shultz et al. (2021).

HD 156424 is a B2V star, and is known to be magnetic with a measured field strength of 0.8 kG (Alecian et al. 2014; Shultz et al. 2018; Shultz et al. 2021). In addition, the star has been observed to undergo rapid radial velocity variation (Alecian et al. 2014), and based on TESS observations, Shultz et al. (2021) determined that this star is indeed both magnetic and pulsating.

A companion star is observed in speckle observations, with an angular separation of 0.774 arcsec (Hartkopf et al. 1993), decreasing to 0.3543 arcsec over a period of about 20 years (Tokovinin et al. 2010). The GAIA DR3 positions imply a separation of 0.814 arcsec (Gaia Collaboration et al. 2016, 2023). The distance to this system, based on GAIA DR3 parallax for the primary star, is 1280^{+120}_{-100} pc. This corresponds to a projected separation of 450^{+150}_{-90} AU. However, it should be noted that GAIA cites a parallax of 0.7810 ± 0.0663 mas for HD 156424A and a parallax of 0.6578 ± 0.1002 mas for HD 156424B (Gaia Collaboration et al. 2016, 2023). These two overlap in the range 0.7147-0.758 mas. The average distance to the system is thus 1360 pc, giving a projected separation of 480 AU, assuming a smaller angular separation of 0.3543 arcsec.

The companion (HD156424B) has also been shown to be magnetic with a field strength of about 1.6 kG Shultz et al. (2021). Based on luminosity estimates from the 2.5 magnitude difference in the y-band (Tokovinin et al. 2010), this star should be about a 5-6 $M_\odot$ main sequence star. Shultz et al. (2021) also find a previously undetected companion, with a mass of at least 1 $M_\odot$ assuming that the eccentricity is 0 and the orbital period is approximately 5 years.

HD 156424 is one of the few doubly magnetic hot binary stars, and the addition of pulsations make this a fascinating target for asteroseismology. There have been relatively few magnetoasteroseismic studies of magnetic pulsating hot stars thus far, in part due to the small number of suitable stars detected. In fact, only a handful of stars have had significant magnetoasteroseismic analysis performed (eg., HD 43317, Buysschaert et al. 2017, 2018; Lecoanet et al. 2022). Neiner et al. (2021) has identified a number of candidate hot magnetic stars, including an estimated 25 that show pulsation signals in TESS data. These pulsating magnetic stars are excellent candidates for detailed magnetoasterosiesmology, although no analysis have been performed on these stars as yet.

Corresponding author: C.C. Lovekin
clovekin@mta.ca

More recently, Shen et al. (2023) performed a variability study of a large sample of magnetic hot stars, identifying several rotating variable stars. Their sample of 118 stars included 10 with coherent pulsation, including HD 156424, and all 10 stars were previously known to be pulsating. They analyzed stochastic low-frequency variability (SLF) in all non-binary stars in their sample, and were able to fit several parameters for the stars in their sample. They conclude that SLF variations are common in hot magnetic stars. The frequency of SLF is typically ≤ 6.3 d^{-1}, well below the range of $p-$mode frequencies expected in β Cephei stars. The characteristic frequency identified for HD 156424 is $\nu_{char} = 0.21 \pm 0.07$ d^{-1}, which is much lower than the frequencies studied in this work.

Chojnowski et al. (2022) and Jayaraman et al. (2022) also detect stars which show some similarity to HD 156424. HD 135348 (Jayaraman et al. 2022) shows evidence of a rigidly rotating magnetosphere (RRM), but does not show strong evidence of pulsation in the TESS lightcurve. Similarly, Tr16-26 (Chojnowski et al. 2022) also has a RRM, but the low scatter in the TESS light curve suggests it is not pulsating, or at least not at significant amplitude. Thus, although these stars are broadly similar to HD 156424, the potential for magnetoasteroseismology of these stars is low.

Magnetoasterosiesmology has been used successfully in other regions of the HR diagram. For example, Li et al. (2022) discovered magnetic fields in the deep interiors of 3 red giant stars, and 10 more were detected by Deheuvels et al. (2023). Coupling between gravity and pressure modes forms mixed modes, which allows stars to be probed near the surface and in the core as rotation and magnetism cause splitting of the frequencies (Mathis & Bugnet 2023; Rui et al. 2023; Loi 2020, 2021; Mathis et al. 2021; Lecoanet et al. 2022). This is usually done for red giants, however MS pulsators can have g-modes that extend to the surface, allowing them to be examined similarly (Rui et al. 2023). In this way, Lecoanet et al. (2022) use asteroseismology to determine the interior magnetic field strength of a slowly pulsating B star.

In this work, we further investigate the pulsation properties of HD 156424, including full asteroseismic modelling of both the primary and the secondary component. The TESS observations and analysis in Section 2 and our models are discussed in Section 3. The results of our modelling are outlined in Section 4, and we summarize our results in Section 5.

2. PHOTOMETRIC ANALYSIS

HD 156424 has been observed with TESS in sectors 12, 39, 66, 91 and 93. The light curve is clearly variable, as shown in Figure 1. In the original analysis by Shultz et al. (2021), they used TESS data from sector 12 to find 11 significant frequencies, of which 6 were considered possible harmonics or combination frequencies. The strongest of these, at 11.2 c d^{-1} was also detected in spectroscopic data. For clarity, we use $\tilde{f}$ when refering to frequencies found in Shultz et al. (2021) and f to refer to frequencies found in this work.

We extracted photometric light curves from TESS images using the Python code developed by Jonathan Labadie-Bartz (for details, see Labadie-Bartz et al. (2022)). This method uses the *TESS*cut service from MAST to cut-out 24×24 pixels images of HD 156424 and surroundings, along with the Lightkurve Python package (Lightkurve Collaboration et al. 2018) to measure the accumulated flux. We implemented the Principal Component Analysis (PCA) detrending method with five regressors to remove the sky background provided the reduced light curves (LCs) for all five studied sectors. The reduced LCs have been cleaned for outliers showing more than 4-sigma deviations (where the mean value and standard deviation were calculated for a sliding time-window of a given width). To study periodic variability of the derived LCs we have employed the Lomb-Scargle periodogram (VanderPlas 2018) which allowed us to detect the significant periodic signals, and the code Period04 (Lenz & Breger 2004) to measure frequencies, amplitudes, and phases for these signals. The corresponding error bars were calculated with Period04 using Monte-Carlo simulations with 1000 processes. The results for each sector are summarized in Table 1.

We also analyzed the combined light curve, with results shown in Table 2. When analyzing the full light curve, we found a number of closely spaced frequencies that are not present in the individual sector data. For example, frequencies were detected at 10.8617, 10.8635; 13.7751 d^{-1} and 22.5639, 24.64 d^{-1}, all with significant amplitudes. The error bars shown in Table 2 were derived using Monte-Carlo simulations with 5000 processes, and the SNR was calculated considering 2 points in the frequency domain on each side of the studied frequency using the Discrete Fourier Transformation (DFT) of the original data (for details, see Lenz & Breger 2004)

Our results are broadly consistent with the earlier analysis by Shultz et al. (2021). The strongest three frequencies in Tables 1 and 2 matched the f_1, f_2, and f_3 frequencies identified by Shultz et al. (2021), at 11.2, 0.71, and 13.7 d^{-1} respectively. The next strongest frequency, $f_{4,5}$ at 10.8 d^{-1} ($\tilde{f}_4$ in Shultz et al. 2021), is quite variable, with an

Table 1. Frequencies extracted from sectors 12, 39, 66, 91 and 93. Error bars are based on 1000 Monte-Carlo processes.

	Sector 12			Sector 39		Sector 66		Sector 91		Sector 93	
ID	Frequency	Amplitude	SNR	Amplitude	SNR	Amplitude	SNR	Amplitude	SNR	Amplitude	SNR
	(c d^{-1})	(mmag)		(mmag)		(mmag)		(mmag)			
f_1	0.7171 ± 0.0003	2.82 ± 0.04	11.3	2.96 ± 0.02	11.5	2.923 ± 0.009	14.9	2.76 ± 0.02	5.3	2.66 ± 0.02	4.6
f_2	11.2069 ± 0.0003	2.66 ± 0.04	12.3	2.91 ± 0.02	18.0	2.930 ± 0.009	16.8	2.92 ± 0.02	4.7	2.96 ± 0.02	4.3
f_3	13.7756 ± 0.0005	1.64 ± 0.04	15.5	2.16 ± 0.02	17.9	1.576 ± 0.009	18.2	1.42 ± 0.02	5.7	1.62 ± 0.02	5.2
$f_{4,5}$	10.8626 ± 0.0013	1.44 ± 0.04	6.7	0.16 ± 0.02	1.0	0.775 ± 0.009	4.5	1.59 ± 0.03	2.5	1.52 ± 0.02	2.2
f_6	22.36 ± 0.01	0.11 ± 0.04	2.7	0.10 ± 0.02	5.3	0.120 ± 0.009	8.2	0.18 ± 0.02	3.5	0.11 ± 0.02	3.2

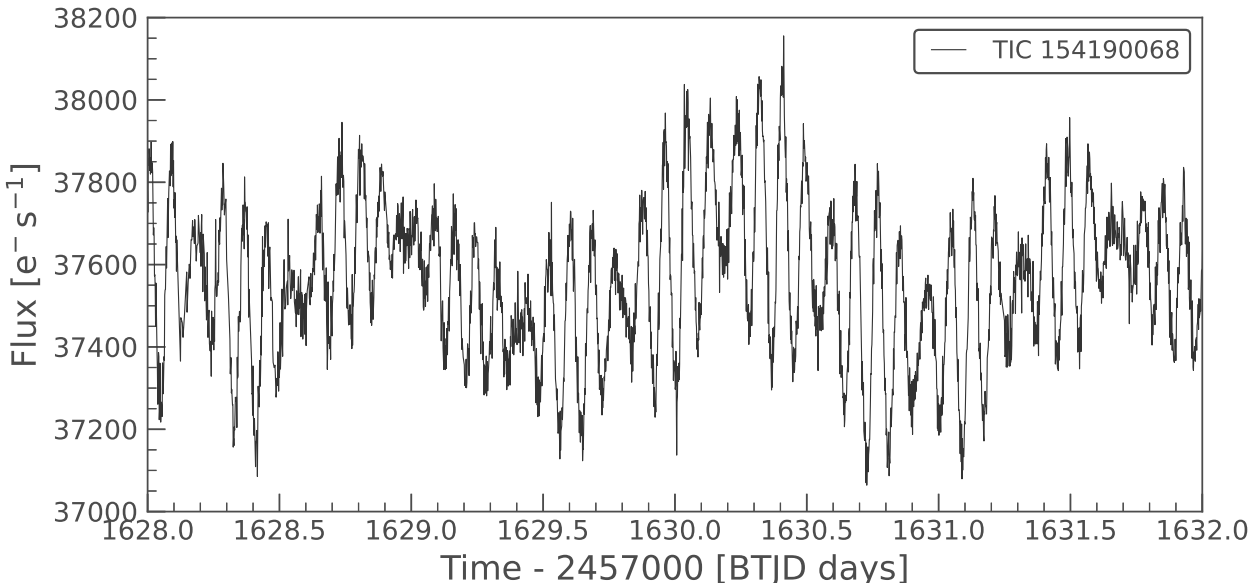

Figure 1. A four day segment of the TESS lightcurve from sector 12.

amplitude dropping from 1.44 mmag in sector 12 to 0.16 mmag in sector 39, increasing to 0.77 mmag in sector 66 and to 1.59 mmag in sector 91, and remains almost at the same level of 1.52 mmag in sector 93. We also found some variability in the amplitude of f_3. The variability in f_3 and $f_{4,5}$ is reflected in the close frequency pairs identified in the combined light curve. The variability of $f_{4,5}$ in sector 93 is illustrated in Figure 2.

We do not detect several of the proposed combination frequencies previously identified by Shultz et al. (2021), including their $\tilde{f}_5$, $\tilde{f}_6$, or $\tilde{f}_{10}$. We also do not see a significant frequency at 16.187 c d^{-1} (their $\tilde{f}_9$). In addition, while we do detect their frequency $\tilde{f}_7$ at 22.36 d^{-1}, we find that it is not significant in sectors 12, 91, or 93. This frequency is present at higher significance (although not higher amplitude) in sectors 39 and 66. It is found in the combined light curve, although its amplitude is considerably lower than the amplitudes of other significant frequencies (see Table 2). A nearby frequency at 24.64 d^{-1} in the combined light curve, corresponding to f_8 in Shultz et al. (2021), also has an amplitude and significance much lower than the other significant frequencies, and is not found in the data from individual sectors.

Table 2. As for Table 1 for frequencies extracted from the combined light curve.

ID	Frequency, d^{-1}	Amplitude, mmag	Phase	SNR
f_1	0.7167423 $\pm 8 \times 10^{-7}$	2.862 ± 0.005	0.3238 ± 0.0005	19.2
f_2	11.2067557 $\pm 4 \times 10^{-7}$	2.909 ± 0.007	0.1084 ± 0.0004	19.9
f_3	13.775093 $\pm 9 \times 10^{-6}$	1.74 ± 0.03	0.811 ± 0.005	25.3
f_4	10.8617 ± 0.004	0.78 ± 0.07	0.74 ± 0.16	5.4
f_5	10.8636 ± 0.001	0.59 ± 0.03	0.72 ± 0.14	4.1
f_6	22.36594 ± 0.00002	0.113 ± 0.009	0.29 ± 0.01	9.9
f_7	24.64 ± 0.02	0.04 ± 0.01	0.71 ± 0.22	4.2

Shultz et al. (2021) proposed that the frequency at 0.716 d^{-1} is either the rotation frequency, or, based on previous measurements (Shultz et al. 2018), that this could be $2f_{rot}$. Our results show that the light curve can be phased on the frequency $f_1 = 0.7167$ d^{-1}, consistent with rotational modulation, as shown in Figure 3 for sector 66. As a further test, we pre-whitened the light curve of all frequencies greater than 10 d^{-1}, and then phased the resulting light curve

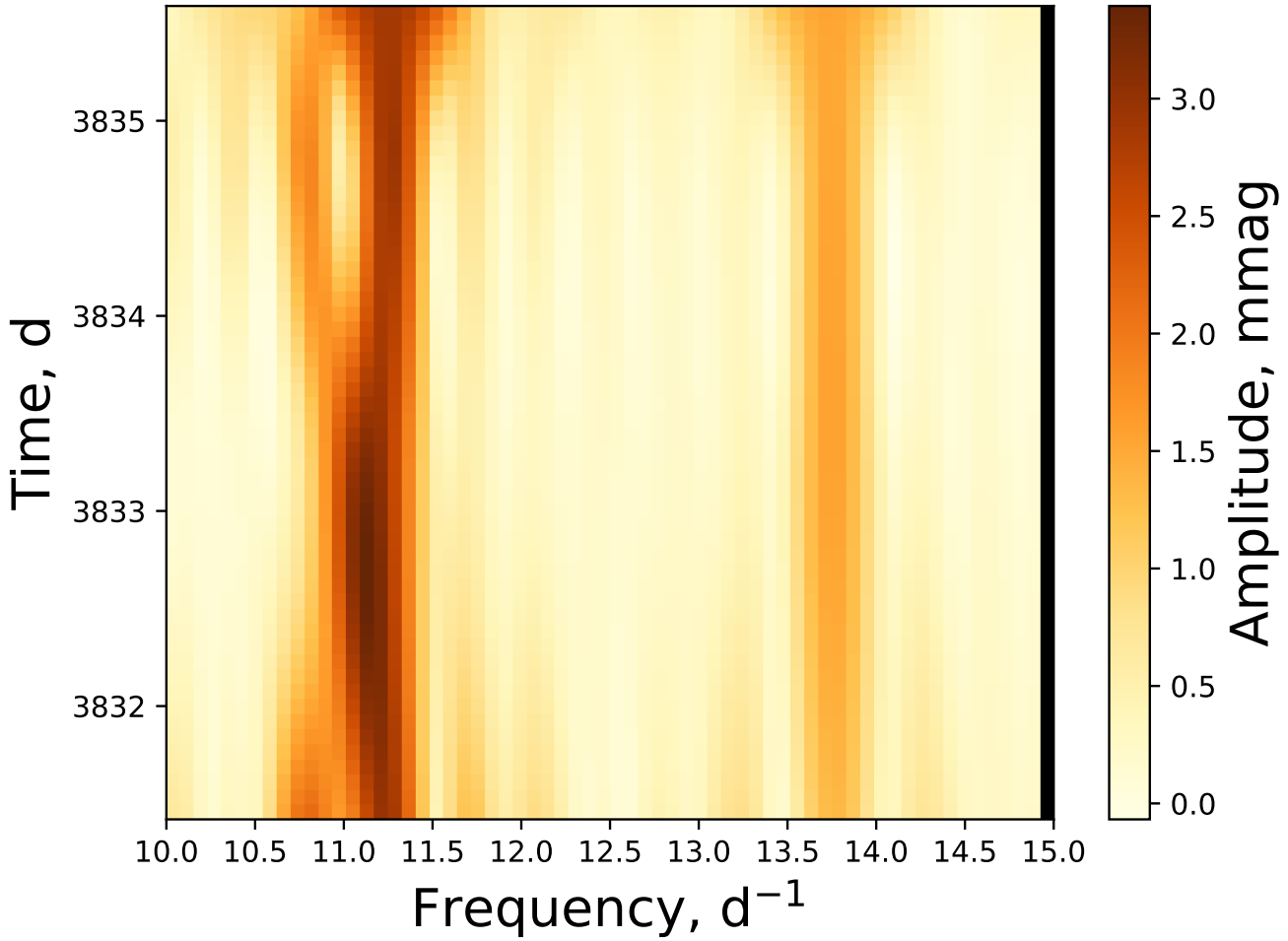

Figure 2. A river plot showing the amplitude of the frequencies in the range 10-15 d^{-1} over sector 93. Each horizontal slice corresponds to a 2.9-day chunk of the light curve. The variability near 10.86 d^{-1} is particularly prominent in this sector.

on f_1. The resulting light curve clearly shows only a single wave, suggesting that f_1 does indeed correspond to the rotation frequency.

If Shultz et al. (2018) is correct and the rotation period of this star is about 2.8 d, then the rotational modulation needs to be a nearly perfect double wave, as there is no evidence of a significant frequency at $f_1/2$ in the periodogram derived for any of the studied sectors or for the combined light curve. Indeed, in their analysis, Shultz et al. (2018) note that the variation in the magnetic field is small compared to the error bars, and the FAP of the $\langle B_z \rangle$ peaks in the period spectrum is quite low. However, as discussed below (see Section 2.1), a frequency of $f_1/2 \approx 0.35$ d^{-1} arises in other places, which may support the hypothesis of a more slowly rotating star.

The rotation frequency proposed by Shultz et al. (2018) of 0.35 d^{-1} does correspond to the separations between f_2 and $f_{4,5}$ (see Table 1). Of these two frequencies, the amplitude of f_2 is very consistent over the five observed sectors. At the same time, the very close frequencies f_4 and f_5 only appear in the combined light curve, and each individual sector only shows a single significant frequency near 10.86 d^{-1}. The amplitude of this frequency is also extremely variable, almost disappearing entirely in sectors 29 and 66. As discussed in §2.1.1, there does appear to be beating between f_2 and $f_{4,5}$ with a beat frequency that is approximately $f_1/2$. While f_2 shows the smooth phase variation expected from beating, the phase variation in $f_{4,5}$ is more complex, and may have other origins. It seems that the relationship between frequencies $f_{4,5}$ and f_2, is complex, and the correspondence between the rotation frequency and the separation is a coincidence rather than rotational splitting.

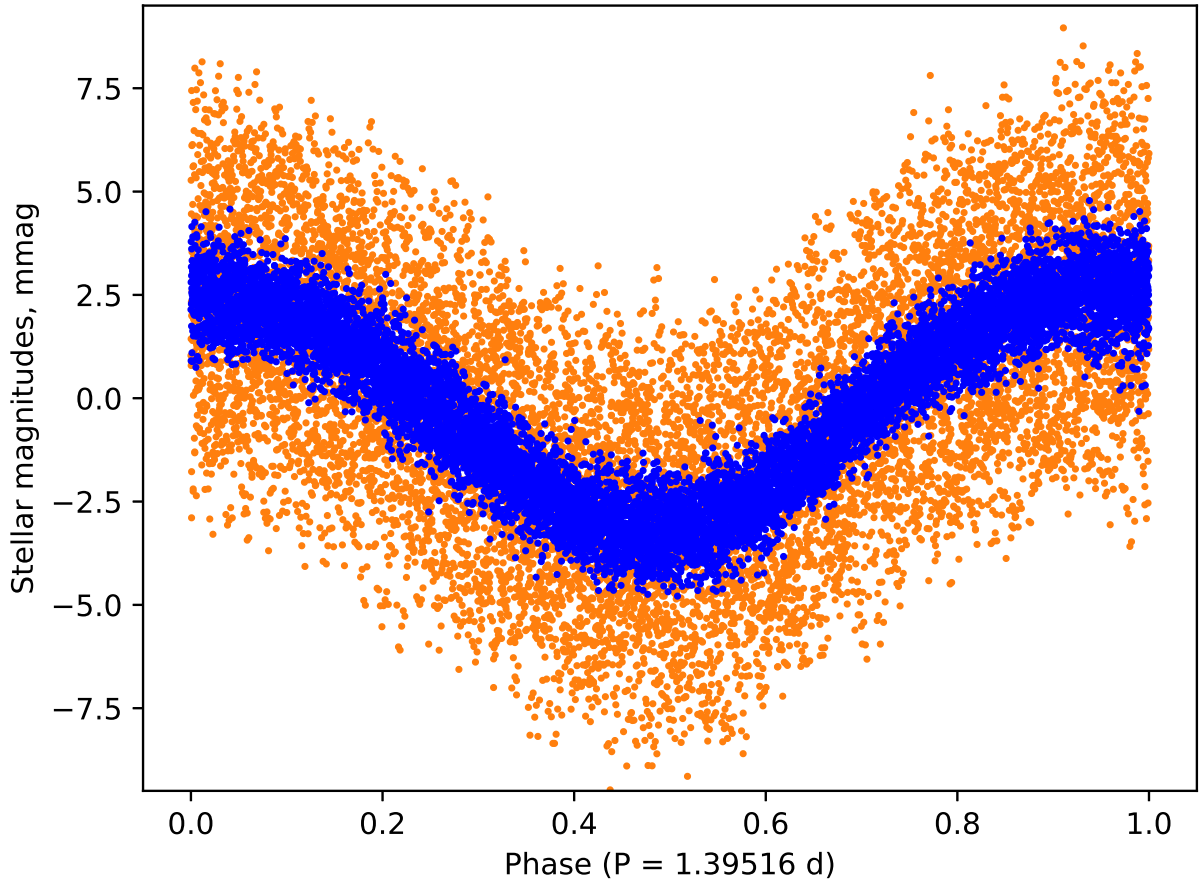

Figure 3. The Sector 66 light curve of HD 156424, phased on a period of 1.3954 d (orange points), corresponding to the frequency $f_1 = 0.7167$ d^{-1}. The orange points are the original lightcurve, while the blue points are the phased light curve after pre-whitening all frequencies > 10 d^{-1}.

Based on our analysis of the TESS data for HD 156424, we restrict our frequency modelling in Section 4 to the four significant p-mode frequencies f_2, f_3, f_4, f_6 found in our data, as given in Table 2. We exclude f_7 from the analysis since it does not appear in any of the individual sectors (see Table 1), and we assume that f_1 is the rotation frequency of the star.

2.1. *Phase Modulation*

As discussed above, HD 156424 is a known binary star, with the two components separated by about 0.35" - 0.77" (Hartkopf et al. 1993; Tokovinin et al. 2010). Shultz et al. (2021) also propose the existence of a third element in the system, based on radial velocity variability. This companion is thought to have much lower mass, with an upper limit of about 1 $M_\odot$, assuming an orbital period of about 5 years. Our observed TESS data span a total period of about 4 years, and so we checked our data for evidence of this low-mass companion. Following the method of Murphy et al. (2014), we divided the light curve into bins and calculated the Lomb-Scargle periodogram for each bin, using a fixed reference point for the phase each time. We started with bins of 0.64 d to study short term variations within each sector. Then, based on the resulting variation, we re-binned the data to 5.8 d intervals to address the longer term variations in phase.

2.1.1. *Short-term Variability*

Within each sector, we divided our data into 0.64-day bins and calculated the phase and amplitude of each frequency and looked at the variation in phase with time. We found significant short-term variability in all frequencies. This is shown for $f_2 = 11.207$ d^{-1} and $f_{4,5} = 10.863$ d^{-1} in Figure 4. In most cases, the phase variability clearly appears to be periodic, with periods that were consistent across all five sectors of the TESS data. Both f_2 and $f_{4,5}$ show consistent variation of phases with a period of approximately 2.889 d (0.346 d^{-1}), which is close to 2.79 d ($f_1/2$), however there is substantially more scatter in the phase plot if f_1 or $f_1/2$ are used to phase the data.

It is possible that the difference between the period of the phase variability and the rotation period is due to differential rotation between the driving regions for the f_2 and $f_{4,5}$ modes and the surface of the star. In our models, the driving region for these modes is quite close to the surface, concentrated in the outer 2.5% of the stellar radius, with a peak around 0.975 R. If the 2.889 d period corresponds to rotation at this depth, while the observed 0.1767 d^{-1} rotation frequency= 1.39516 d rotation period corresponds to surface features, then the sub-surface region of the star would be rotating more slowly than the surface. This is true even if the true rotation period is $f_1/2$, in which case the rotation period would be 2.790 d. It is hard to imagine effective angular transport mechanisms in the presence of a magnetic field that could produce this kind of profile.

Differential surface rotation has been previously detected in magnetic Am stars (e.g. Blazère et al. 2020) as a result of magnetic shear across the surface, and it is possible a similar effect is seen here. In this case, the differential rotation would be between the pole and the equator. Rotation is known to confine pulsation modes to the equatorial regions of the star (e.g. Reese 2022), and so the 2.889 d period would most likely be the equatorial rotation period. The observed rotational modulation at f_1 would then be the result of surface features closer to the poles.

The phase variation in f_2 is smooth when phased over a period of 2.889 d. This period was estimated using DFT analysis of phases found for f_2 using the 0.64-day bins. This smooth variation is expected to arise from beating between frequencies. The beat frequency, 0.346 d^{-1}, is approximately the same as the difference between f_2 and $f_{4,5}$. However, while f_2 shows smooth variation with phase, $f_{4,5}$ does not (see Figure 4).

Over each cycle, the phase of $f_{4,5}$ rises from 0 to a maximum and then drops back to 0 before repeating, as shown in Figure 4. This variation is consistent across all five sectors, and clearly phases with a period of 2.889 d. This is consistent with the type of variation seen in an oblique pulsator model (Bigot & Dziembowski 2002; Bigot & Kurtz 2011). If the strength of the magnetic field is comparable to the magnetic field, the pulsation axis of the dipole modes will not align with either axis. As a result, the observed amplitude of the mode varies as the star rotates. Bigot & Kurtz (2011) show that the amplitude and phase of the star pulsating at a frequency ω are expected to vary as

$$\frac{\delta L}{L}(t) \propto R(t)\cos(\Omega t - \Psi(t)) \tag{1}$$

where

$$R(t) = \sqrt{A^2 + B^2} \tag{2}$$

and

$$\Psi(t) = \arctan\left(\frac{B}{A}\right). \tag{3}$$

The functions A and B are defined as

$$A = \cos\psi\,(\cos\gamma\cos i + \sin\gamma\sin i\cos(\Omega t)) \tag{4}$$

$$B = \sin\psi\sin i\sin(\Omega t) \tag{5}$$

where i is the inclination of the system, Ω is the angular rotation velocity of the star, γ is the angle between the rotation axis and the plane of the ellipse, and ψ is the polarization axis, defined by the ratio of the two axes of the ellipse.

We attempted to fit our data for the phase variation of $f_{4,5}$ to the oblique pulsator model derived in Bigot & Kurtz (2011), which assumes the observed pulsation is a dipole mode. We used the Python package `dynesty` (Koposov et al. 2022; Speagle 2020; Skilling 2004) to explore the parameter space with nested sampling. We ran models allowing the three main variables in Bigot & Kurtz (2011) to be free parameters: ψ, which measures the ratio of the axes of the elliptical motion; γ, which is the inclination of the X axis of the ellipse with respect to the rotation axis; and i, the angle between the rotation axis and the line of sight.

We found that to reliably fit the data, we needed to set $\Omega = 1.0874$ rad s^{-1}, which corresponds to a period that is approximately twice the phase period shown in Figure 4, or four times slower than the proposed rotation frequency

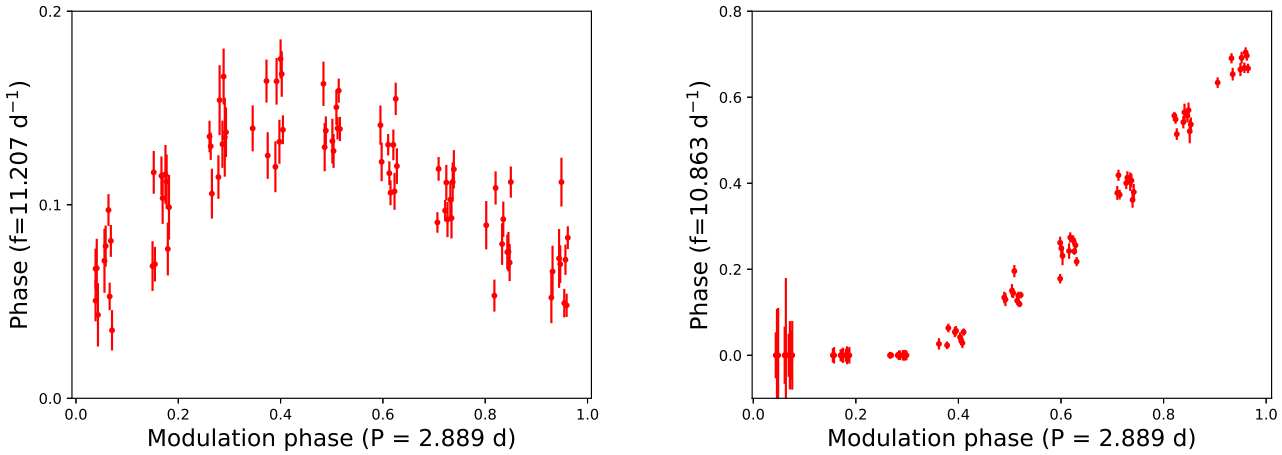

Figure 4. Left panel: phase variation of f_2 during sector 66 (see Table 1), phased over a period of 2.889 d. Right panel: the same, but for $f_{4,5}$. Phases are calculated in 0.64-day bins for sector 66. These variations are periodic with a frequency of 0.346 d^{-1}, which is approximately $f_1/2$, in agreement with the rotation period of the star from magnetic data (Shultz et al. 2018). The rise in phase and sharp drop over each cycle can be clearly seen in the right panel. The zero phase is chosen separately for each frequency to ensure that the phase minimum occurs at the zero of the modulation phase.

of the star (f_1). It is not clear how to account for this discrepancy in rotation period. We derived best-fit parameters of $\psi = 0.14^{+0.01}_{-0.08}$, $\gamma = 1.21^{+0.31}_{-0.77}$, and $i = 1.08^{+0.40}_{-0.82}$ radians, which correspond to $\psi = 7.5°$, $\gamma = 65.5°$, and $i = 57.8°$. We repeated this process for sector 66, which also shows the same behaviour. Our fits in that sector were similar, and agree with the sector 12 values within errors. The comparison between our phase data and the resulting fit is shown in Figure 5.

We found that there were clear non-linear correlations between the variables, as shown in Figure 6. In particular, the best fit value of both γ and ψ are strongly dependent on the inclination of the system.

The oblique rotator model (Stibbs 1950) also predicts that the observed mean longitudinal magnetic field will vary according to the expression :

$$\langle B_z \rangle \propto \cos\beta\cos i + \sin\beta\sin i\cos\Omega t. \tag{6}$$

Shultz et al. (2021) did not report any strong variation in the magnetic field of HD 156424. This is not in conflict with the oblique pulsator model, as they report $\beta < 20°$, which would make the amplitude of the variation ($\propto \sin\beta$) quite small.

The phase variation in f_3 is also smooth, but the period of phase variability is not the same as the period in f_2 and $f_{4,5}$, and also changes from sector to sector, ranging from $P = 1.857$ d (sector 66) to $P = 2.883$ d (sector 12). None of these periodicities shows any relationship to the rotation frequency. The last frequency, f_6, also shows some short-term phase variability, but relatively large errors in the phase determinations make it difficult to accurately detect any regular variation in the phase.

2.1.2. *Long-term Variability*

We also combined our phase determinations to look for longer-term trends in our data. In this case we fit the phase variability derived using 5.8-day bins, chosen to ensure we were averaging over longer time spans than the longest period observed in the short-term phase variability data. We then fit the resulting phase data for each frequency to a sinusoid,

$$y = a * \sin(2\pi bt + c) + d \tag{7}$$

using a weighted least-squares fit. The strongest variation is observed in f_2 which is well fit by a sinusoidal function with a period of 7400^{+14000}_{-5200} d (20.3 years). The phase measurements and sinusoidal fit for f_2 are shown in Figure 7. The variation in f_3 is much longer, with a period of nearly 300,000 years. The errors and amplitude of the fit are extremely uncertain in this case, and the fit is also consistent with a flat line ($a = 22 \pm 1.87 \times 10^5$).

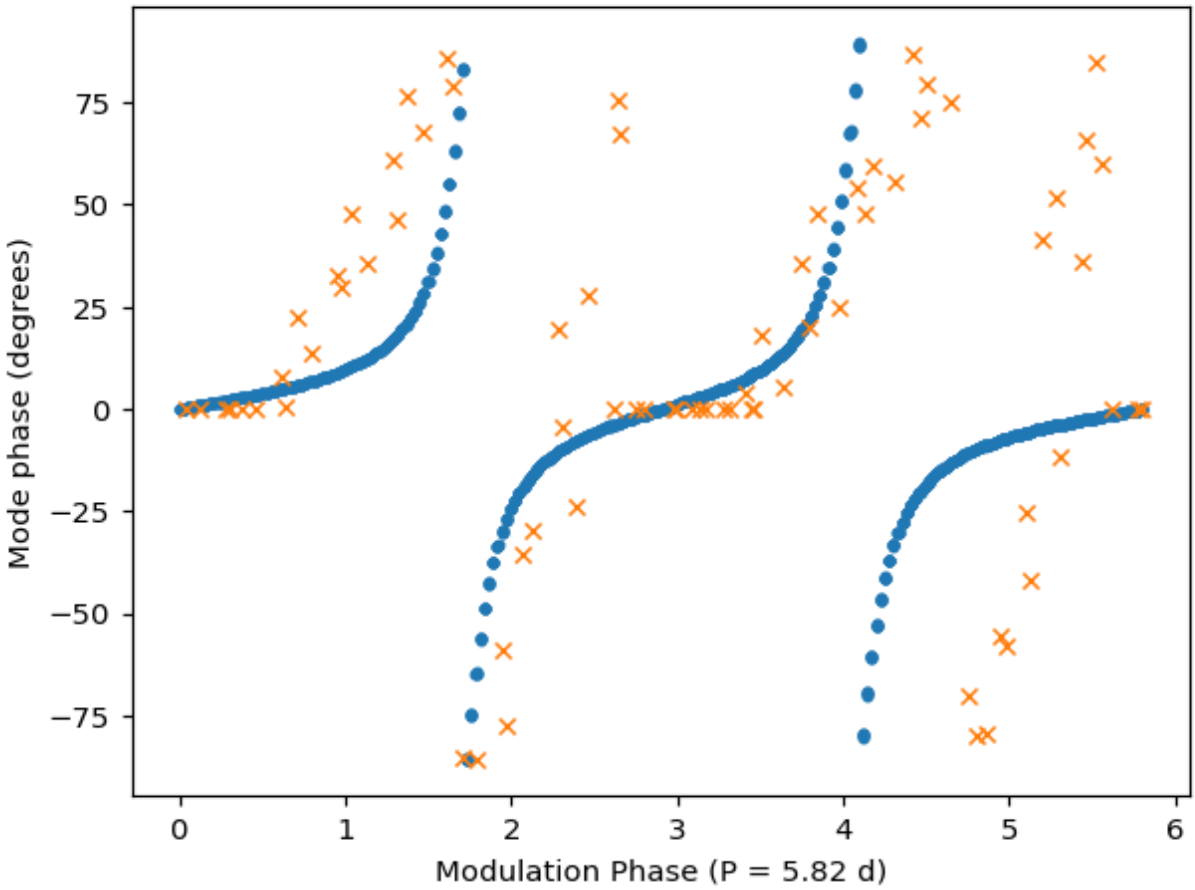

Figure 5. The comparison between the oblique rotator model (blue) using values of $\psi = 0.14^{+0.01}_{-0.08}$, $\gamma = 1.21^{+0.31}_{-0.77}$, and $i = 1.08^{+0.40}_{-0.82}$ rad, the best-fitting parameters as determined from the nested sampling analysis. The phase data for $f_{4,5}$ are shown for sector 12 (orange x).

The third frequency with phase variability significant enough to check for long-term variability was $f_{4,5}$, which was well fit by sinusoidal variation and a period of 1490 ± 10d (4.0 years). This last period is in closest agreement with the 5-year period proposed by Shultz et al. (2021).

We generated artificial radial velocity curves for each frequency based on our fits by converting our phase differences to time delays and then taking the derivative (see Murphy et al. 2014, for more details). For f_2 we found a peak amplitude of 155 ± 5 m s^{-1}, and f_3 gives a maxiumum radial velocity of about 90 m s^{-1}. However, the radial velocity curve in this case has clearly not reached a maximum value, but shows a linear change over the period of the TESS observations. For $f_{4,5}$ the amplitude of the radial velocity curve is much larger, with a peak of 6000 m s^{-1}. In comparison, Shultz et al. (2018) give a radial velocity of 8000 ± 1000 m s^{-1} for the star. It seems that the parameters we derive for the phase velocity of $f_{4,5}$ are in closest agreement with these previous values.

Combined with our best fit model mass of 9.8 M$_\odot$ (see §4), a maximum radial velocity of 120 m/s, and a period of 20.3 years (7400 d), iteratively solving the binary mass function gives an upper mass limit of 0.05 $M_\odot$ for the proposed third element, assuming $i = 0$ and $e = 0$. This would place the companion 15 AU from the primary star. If we assume the higher radial velocity and shorter period associated with $f_{4,5}$ is correct, the companion mass rises to 1.6 M$\odot$, located a distance of 5 AU from the primary. In either case, the companion is much lower mass than the primary and would not be easily visible in either spectroscopy or photometry. In fact, if the parameters associated with f_2 are

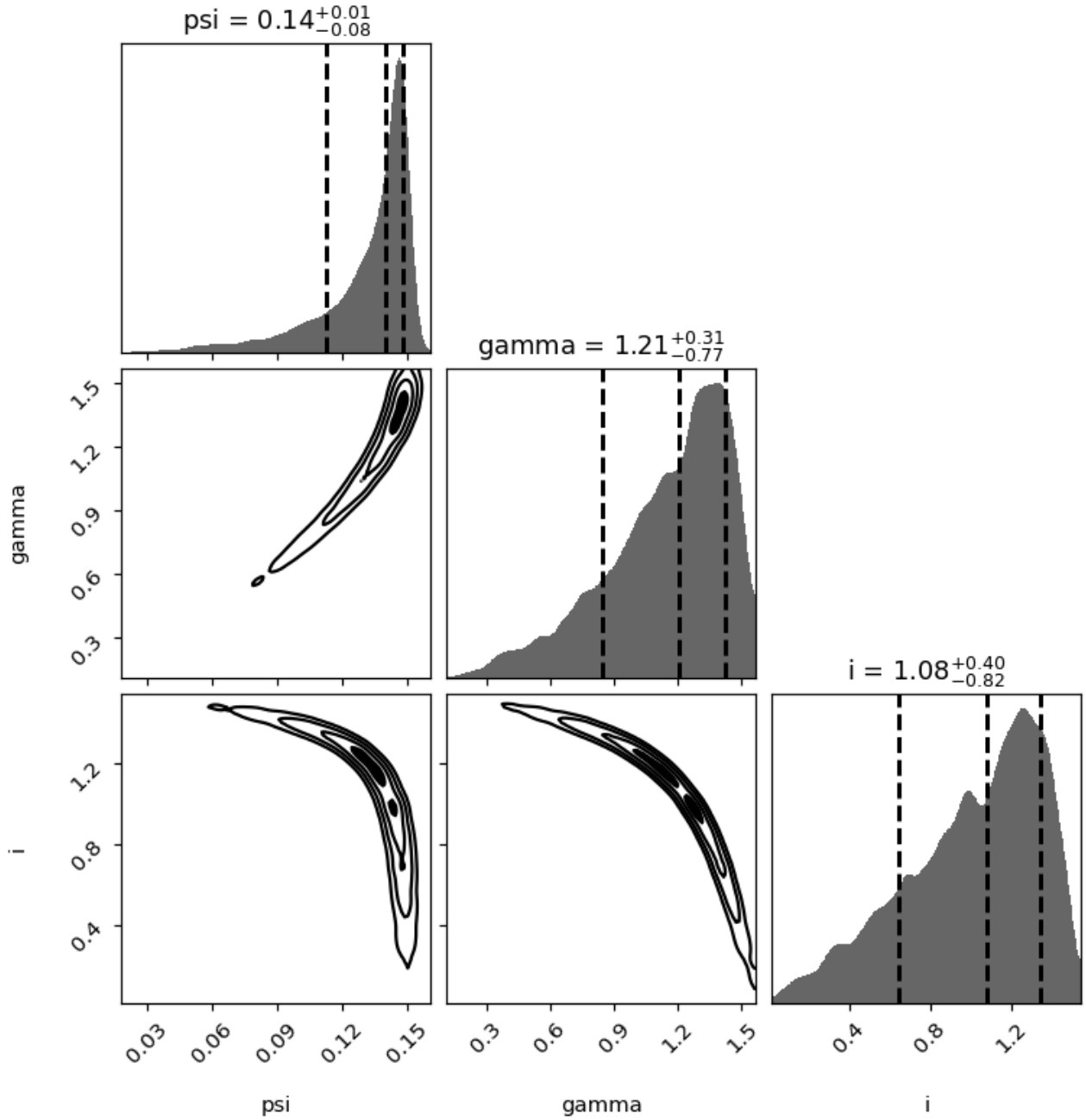

Figure 6. Correlations from our nested sampling of the parameters Ψ, γ, and i for fits to the phase variation of $f_{4,5}$ over sector 12. Best fit parameters are given above the histograms in radians.

correct, the companion may be a brown dwarf or hot Jupiter rather than a star. Either way, we do not expect the companion to have a significant effect on the evolution of the primary star.

3. ASTEROSEISMIC MODELS

To model these stars we used Modules for Experiments in Stellar Astrophysics (MESA) version 15140 (Paxton et al. 2011, 2013, 2015, 2018, 2019) with the modified torque and wind routines developed by Keszthelyi et al. (2020) to include the effects of fossil magnetic fields. The mass loss and stellar winds were also implemented by these routines. We ran grids at metallicities Z = 0.014, 0.02, 0.03, and 0.04 with masses between 8.0-10.0 $M_\odot$. We used a mixing

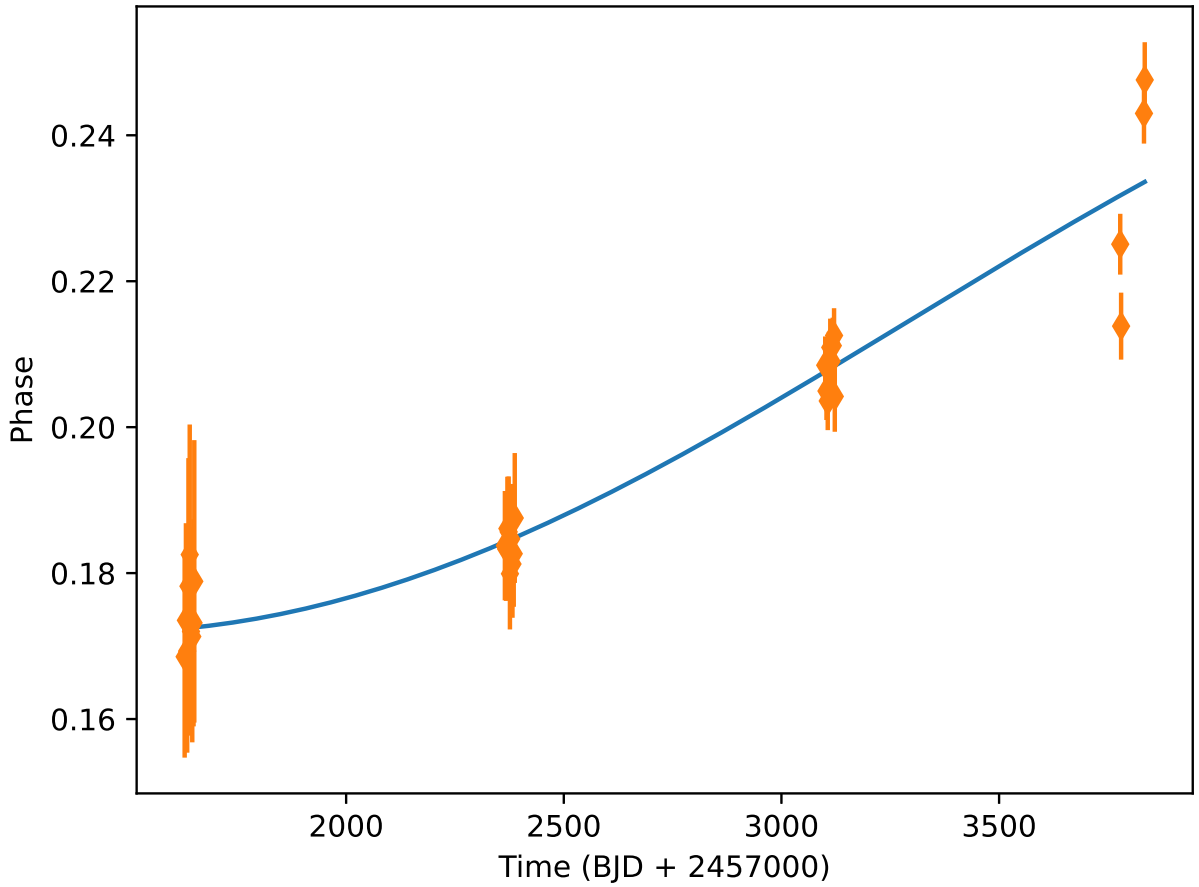

Figure 7. The long-term phase variation in f_2 derived using 5.9 d sampling bins fits to a sinusoid (Eqn. 7). The best fit suggests a long term variability with a period of 7400 d (20.3 years).

length parameter of 2 and no convective overshoot. Rotation was imposed on the ZAMS at rates between 100-350 km s^{-1} and magnetic fields of strengths 770-870 G, consistent with the observed magnetic field strength. The parameter range and step size used in each grid is summarized in Table 3. We used a magnetic braking efficiency of 1 and a constant field evolution, meaning that the magnetic field strength remains constant over the evolution of the star. We also used the uniform torque method, in which angular momentum lost from the star is removed from the total angular momentum reservoir rather than only the near-surface layers.

We modelled the primary and secondary separately. With a projected separation of 450 AU, the two stars are expected to have evolved independently, and there is no need to include the effects of binarity. The presence of the third low-mass component is also not expected to affect the evolution of the two magnetic stars. With the proposed limits of a 1 $M_\odot$ companion in a 5 year orbit, the semi-major axis is predicted to be around 1.5 AU. Our results suggest the companion may be even smaller and more distant, with a correspondingly smaller effect on the primary. As such, these stars can safely be modelled as single stars. A subset of our evolution grid is shown in Figure 8, along with the observed position of HD 156424 based on values from Shultz et al. (2021).

We saved models every 50 timesteps, giving approximately 5 points along each model main sequence. We then used GYRE version 7.1 (Townsend & Teitler 2013; Townsend et al. 2018; Goldstein & Townsend 2020; Sun et al. 2023) to calculate the adiabatic and non-adiabatic pulsation frequencies in the range 10-25 d^{-1} for each model. for $\ell = 0$, 1, 2, and 3, and $|m| \leq 2$. As discussed above, we assume that $f_1 = 0.718 d^{-1}$ is the rotation frequency, and do not include it in our asteroseismic modelling.

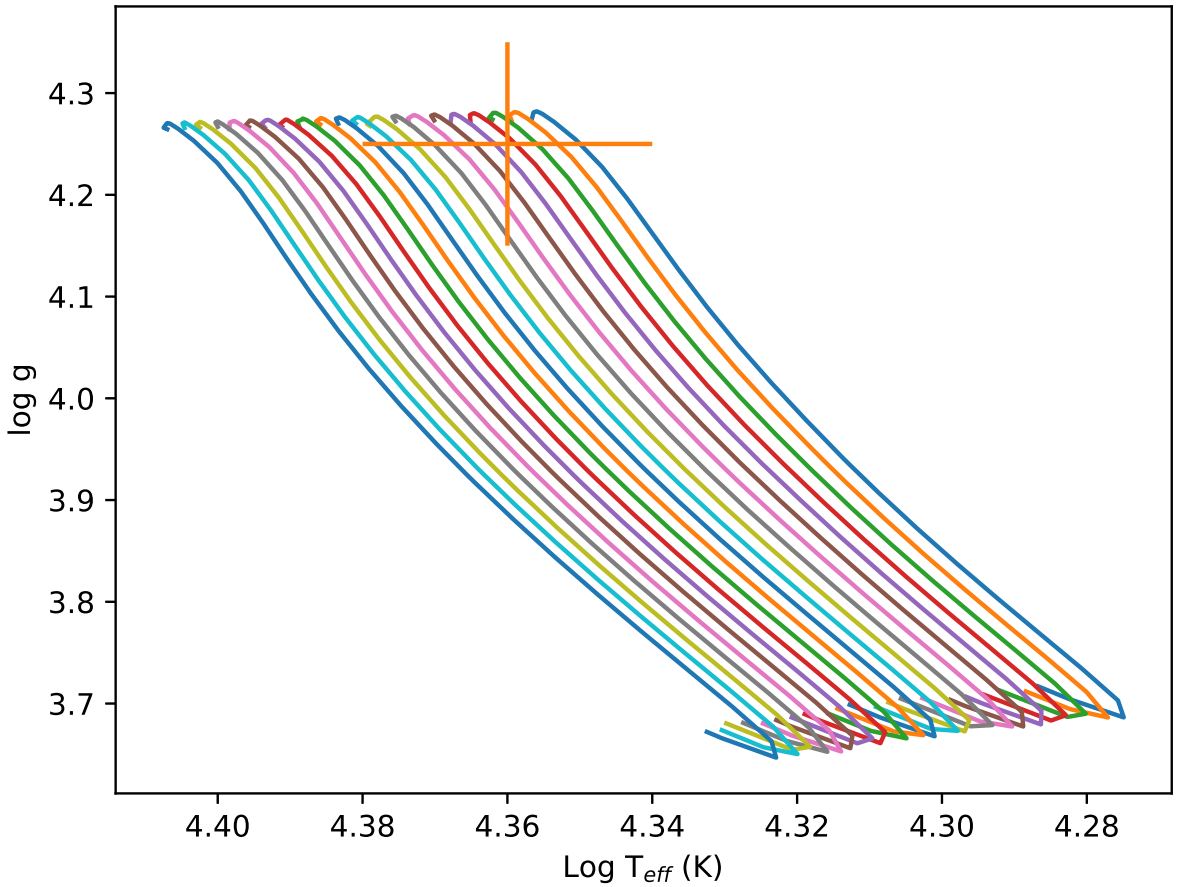

Figure 8. A Kiel diagram showing a subset of our model grid. Shown are models with Z = 0.014, v_{ZAMS} = 200 km s^{-1}, and $\vec{B}$ = 820G. Tracks shown range from 8.0 M$_\odot$ to 10.0 M$_\odot$.

We then ran a similar grid of models of the secondary star with metallicities Z = 0.02, 0.03 and 0.04, masses 4.2-6.0 M$_\odot$, and magnetic field strengths 1500-1700 G. We calculated non-adiabatic pulsation frequencies in the same way for both sets of models.

	primary			secondary		
	min	max	step size	min	max	step size
$v_{\rm rot}$ (km s^{-1})	100	350	50	100	350	50
$M_\star$ (M$_\odot$)	8.0	10.0	0.1	4.2	6.0	0.1
B_0 (G)	770	870	50	1500	1700	100

Table 3. Parameters used for the grids of MESA models of the primary and secondary star.

4. ASTEROSEISMIC FITTING

The observed orbital separation of the A and B components of the system is less than 1" (Hartkopf et al. 1993; Tokovinin et al. 2010), which is well within a single pixel of the TESS observations. The observed light curve is thus a combination of the light from both stars. Based on our phase modulation results, we looked at three different cases: i)

all frequencies are from pulsation in the primary star; ii) all frequencies are from pulsation in the low-mass secondary star; and iii) the frequency f_3 belongs to the secondary star.

First, we assumed that all frequencies (f_2, f_3, $f_{4,5}$, and f_6) were associated with the primary star. In this case, we found a total of 33 models with χ^2 values below 2.5, nearly all of which are from the Z = 0.03 model grid. Higher metallicities were preferred overall, and in the Z = 0.014 grid we found no models that matched the observed frequencies with $\chi^2 < 2.5$. However, the model with the lowest χ^2 was from the Z = 0.02 grid: a 9.8 $M_\odot$ model with an initial rotation velocity of 150 km s^{-1} on the ZAMS, and a magnetic field strength of 770 G. The parameters of the best fitting model are summarized in Table 4. We also found that the asteroseismic fits were relatively insensitive to the strength of the magnetic field, and all three modelled $\vec{B}$ had similar frequency fits. This is not surprising, as we impose a magnetic field strength at the ZAMS. Since our models are so young, the magnetic effects have not had significant time to impact the stellar structure.

Given the model rotation velocity and radius for our best fitting model, we find a theoretical rotation frequency of 0.725 d^{-1}, in good agreement with f_1. This model is also in good agreement with the observed temperature and luminosity of the star, as shown in Figure 9. Our best fit rotation velocity of 146 km s^{-1}, combined with the literature measurement of $v \sin i = 4.4$ km s^{-1} (Shultz et al. 2021), implies an inclination of 1.7°, which would suggest the star is observed nearly pole on. This value is much lower than the best fit derived for the oblique pulsator model in Section 2.1.1.

The comparison to the observed frequencies is shown for our best fitting Z = 0.02 model in Figure 9. We see positive excitation in frequencies below about 15 d^{-1}, and so we can expect f_2, f_3, and $f_{4,5}$ to be driven. There are no frequencies with positive growth rates in the range of f_6. However, as noted in (Shultz et al. 2021), this frequency is approximately $2f_2$, and is likely not an intrinsic frequency. Removing this frequency from our fitting process does not produce a significant change in the distribution of best fit models. At Z = 0.02 and 0.03, the best fit mass decreases slightly, but the fits at Z = 0.04 and 0.014 are unchanged.

	Case 1	Case 2	Case 3	Literature values
Z	0.02	0.02	0.02	
Age (years)	5.76e5	1.36e6	7.97e5	
X_c	0.69	0.70	0.68	
$M_\star$ ($M_\odot$)	9.8	4.5	9.5	8.8 ± 0.6
$v_{\rm ZAMS}$ (km s^{-1})	300	300	100	
$v_{\rm rot}$ (km s^{-1})	146	290	290	4.4±1.5[a]
R ($R_\odot$)	3.98	2.77	4.11	3.8 ± 0.2
B_0 (G)	770	1700	770	820 ± 50
log T	4.39	4.18	4.37	4.36 ± 0.02
log g	4.22	4.21	4.18	4.25
log L	3.72	2.55	3.66	3.5

[a] Published value of $v \sin i$ (Shultz et al. 2021)

Table 4. Properties of the best fitting models. Case 1 assumes that all four p-mode frequencies are associated with the primary, Case 2 assumes they are all associated with the secondary, and Case 3 models the primary with only f_2 and $f_{4,5}$. Literature values are taken from Shultz et al. (2021).

Second (Case 2), we compared the observed frequencies with the models of the secondary star (see Fig. 10). Based on the magnetic models of Shultz et al. (2021), we calculated a grid of models between 4.2 and 6 $M_\odot$. When we compared these models to the observed frequencies, we found that all models of the secondary match poorly, with much higher χ^2 values than the primary models. The secondary star models also have fewer frequencies that are expected to be excited than the primary star models. The best fitting models at each metallicity are shown in Figure 10, and the properties of the best fitting model are summarized in Table 4.

Although we have modeled the secondary star as a 4-6 $M_\odot$ star, it seems likely that it is actually significantly more massive. Tokovinin et al. (2010) cite a magnitude difference of 2.3 mag in the y band which they note is probably overestimated. Shultz et al. (2021) use this magnitude difference to estimate that the companion is dimmer by a factor of about 8 in luminosity. However, the visual magnitudes from the Tycho double star catalogue (Fabricius et al.

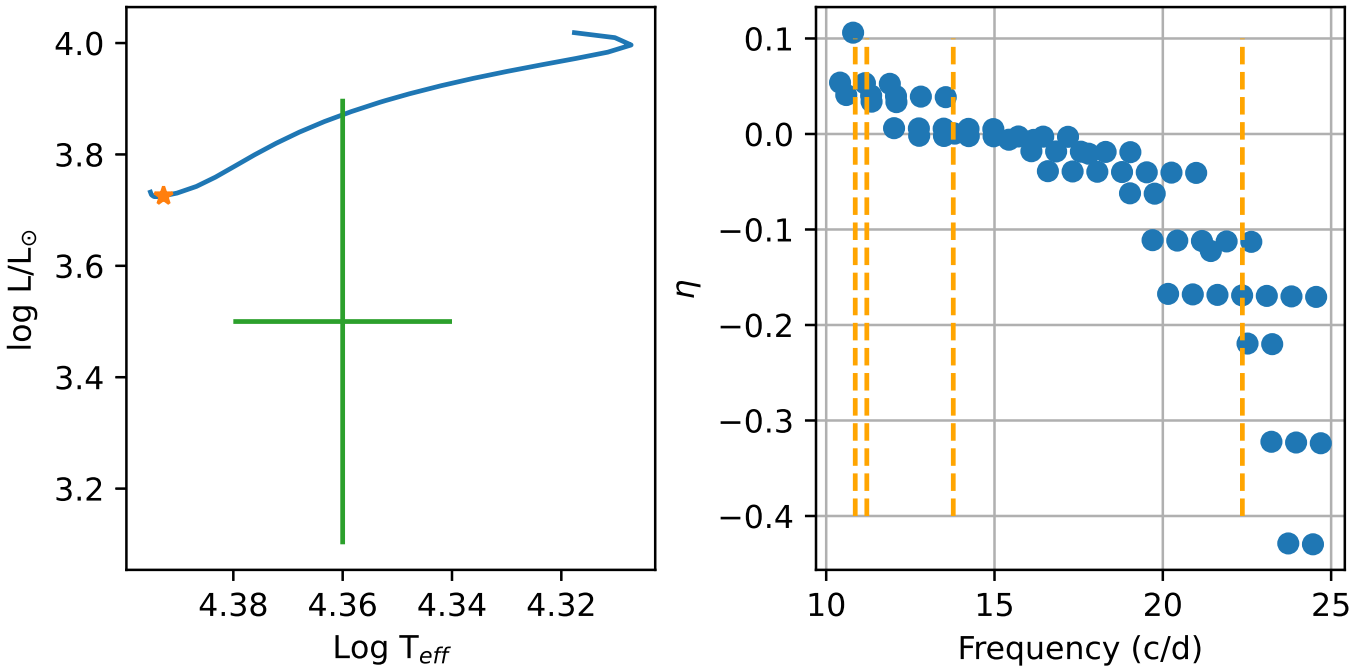

Figure 9. Left: HR diagram of the best fitting Z = 0.02 model of the primary star. The orange star shows the location of the model, and the green error bars indicate the observed location of HD 156424. Right: Predicted mode excitation for the best fitting model in the range 10 to 25 d^{-1}. Vertical dashed lines indicate the location of the 4 primary frequencies from the TESS observations.

2002) give V band magnitudes of 9.24 and 9.75 for the primary and secondary respectively. This difference of 0.51 magnitudes implies the primary is a factor of 1.6 brighter than the secondary, giving the secondary log $L \approx 3.5$. Similar magnitude differences are seen in GAIA DR3 data (Gaia Collaboration et al. 2016, 2023). This magnitude difference suggests the secondary is closer to 7.5-8 $M_\odot$ rather than the 5 $M_\odot$ suggested by Shultz et al. (2021). However, based on ESPaDOnS spectra, (Shultz et al. 2021) found that the pattern of ionization lines is consistent with a much cooler companion, with the effective temperature of the primary at 23,000 K and the secondary at 16,000 K, more consistent with the lower mass range.

Finally (Case 3), we tried dividing up the frequencies between the two stars based on our phase data in Section 2.1.1. Since we see beating between f_2 and $f_{4,5}$, we assume that these two frequencies must be associated with the same star. Since f_6 appears to be $2f_2$, we include it as well, although excluding it does not significantly change our results. This leaves only $f_3 = 13.7 d^{-1}$ as potentially associated with the secondary. With only one frequency, we do not attempt to fit models of the secondary in this case.

When we fit the models in the primary grid to frequencies f_2, $f_{4,5}$, and f_6, we find that our best fit model is slightly less massive and more rapidly rotating than in Case 1, as shown in Table 4. The best fit model in this case is arguably a better fit to the observed temperature and luminosity of HD 156424, as shown in Figure 11. However, given the more rapid rotation rate of this model, the rotation frequency is expected to be 1.39 d^{-1}, nearly double f_1, and does not correspond to any of the frequencies observed in our data.

Overall, our models suggest that the HD156424 system is quite young, and we find that modes in the observed range of p-mode frequencies are not predicted to be excited in the later part of the main sequence for stars in this mass range. Higher metallicity models (Z=0.03 and 0.04) give better fits than the lower metallicity models (Z = 0.014 and 0.02), although our best-fitting individual model in both Case 1 and Case 3 comes from the Z = 0.02 grid. The model in Case 1 in particular is in good agreement with the proposed rotation frequency observed at $f_1 = 0.72$ d^{-1}.

5. CONCLUSIONS

We have analyzed five sectors of TESS observations for HD 156424, both individually and as a combined data set. We found 7 significant frequencies across all sectors, and 5 frequencies that are significant in individual sectors. Of our detected frequencies, the pair f_4 and f_5 are extremely close, and likely indicate frequency variability over the course

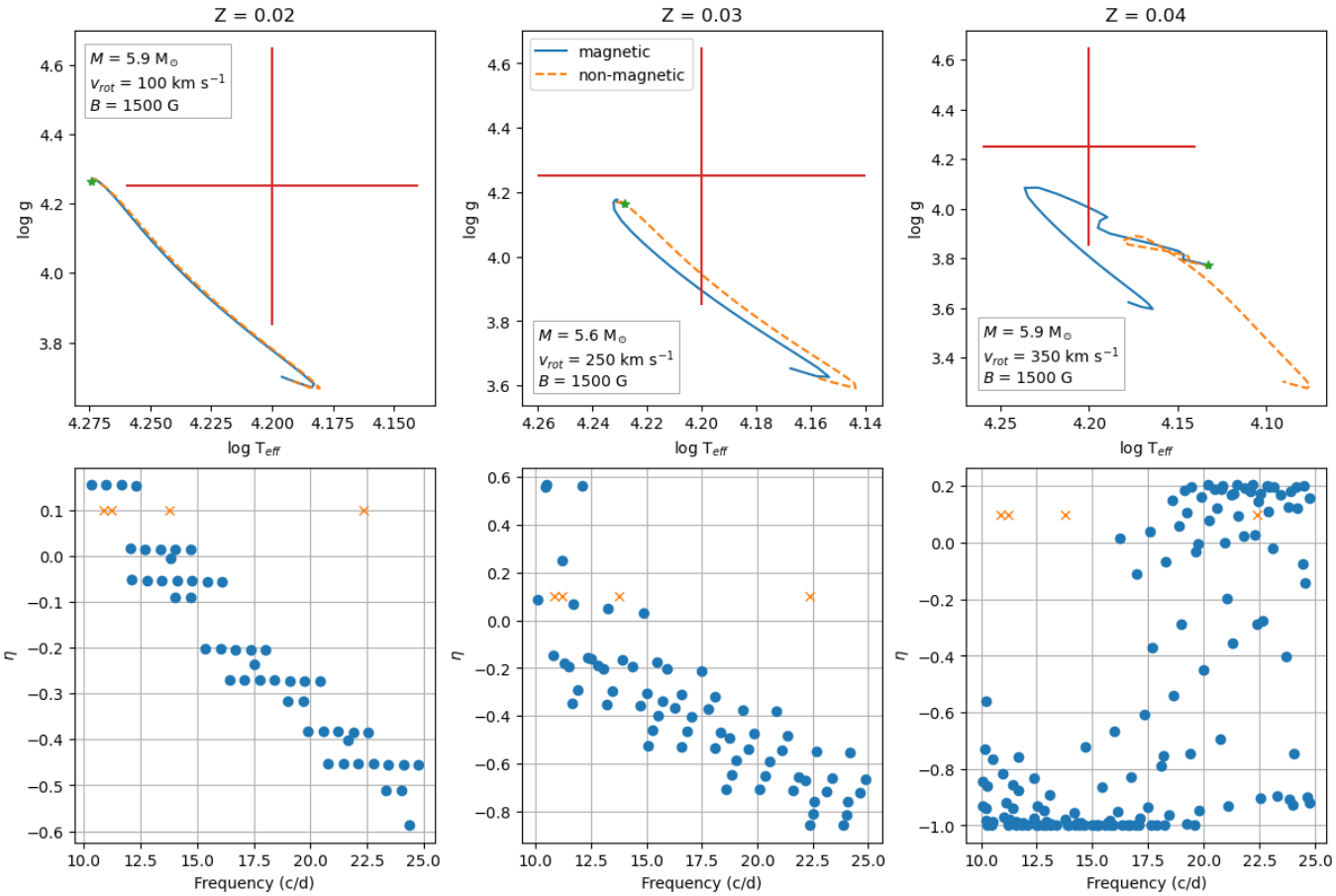

Figure 10. *Needs to be redone to match Figure 9.* As for Figure 9 but for best-fitting models of the secondary star with Z = 0.02, 0.03 and 0.04. The best fitting models are between 5.6 and 5.9 $M_\odot$, depending on the metallicity. The best fitting models are much older than the best fitting models of the primary, and many of the observed modes are not predicted to be excited.

of the TESS observations. For $f_{4,5}$, the amplitude is strongly variable between and within sectors, as shown in Figure 2. We conclude that $f_1 = 0.7171$ d^{-1} likely corresponds to the rotation frequency of the primary, HD 156424A.

Following the method of (Murphy et al. 2014), we divided our light curve into 0.64 d bins and calculated the phase of each pulsation frequency in each bin. We found significant short term variability in f_2, f_3, and $f_{4,5}$. Both f_2 and $f_{4,5}$ have phase modulation with a period of 2.889 d, which is close to, but not exactly $2f_1$. We suggest that this may be the result of differential rotation in the envelope of the star, resulting in a slightly longer rotation period in the driving region of the $p-$modes. Since the driving region in these modes is quite close to the surface, the differential rotation is probably at the surface, with the poles rotating more rapidly than the equator.

We found smooth variation for f_2, which suggests that the variation is caused by beating between modes. The observed beat period of 2.889 d corresponds to the frequency 0.346 d^{-1} which is approximately the separation between f_2 and $f_{4,5}$, suggesting there is beating between these two frequencies. The variation in $f_{4,5}$, although it has the same period as the variation in f_2, shows very different behaviour. There is a gradual increase over each cycle, followed by a sharp drop. This phase behaviour is consistent with the expected behaviour of an oblique magnetic pulsator (Bigot & Dziembowski 2002; Bigot & Kurtz 2011). We were able to fit our data from sector 12 to this model, and found reasonable fits with $\psi = 0.14^{+0.01}_{-0.08}$, $\gamma = 1.21^{+0.31}_{-0.77}$, and $i = 1.08^{+0.40}_{-0.82}$ radians. Fits to the data from sector 66 show agreement within the errors.

We then divided our light curve into 5.8 day bins to look for long-term variability. We found strong long term variations in f_2 and $f_{4,5}$. The period in the phase variation of f_2 was 7400^{+14000}_{-5200} d. The long-term variability of f_2 is strongly modified by the data derived from sector 93. The 4 points of binned data for this sector significantly increases

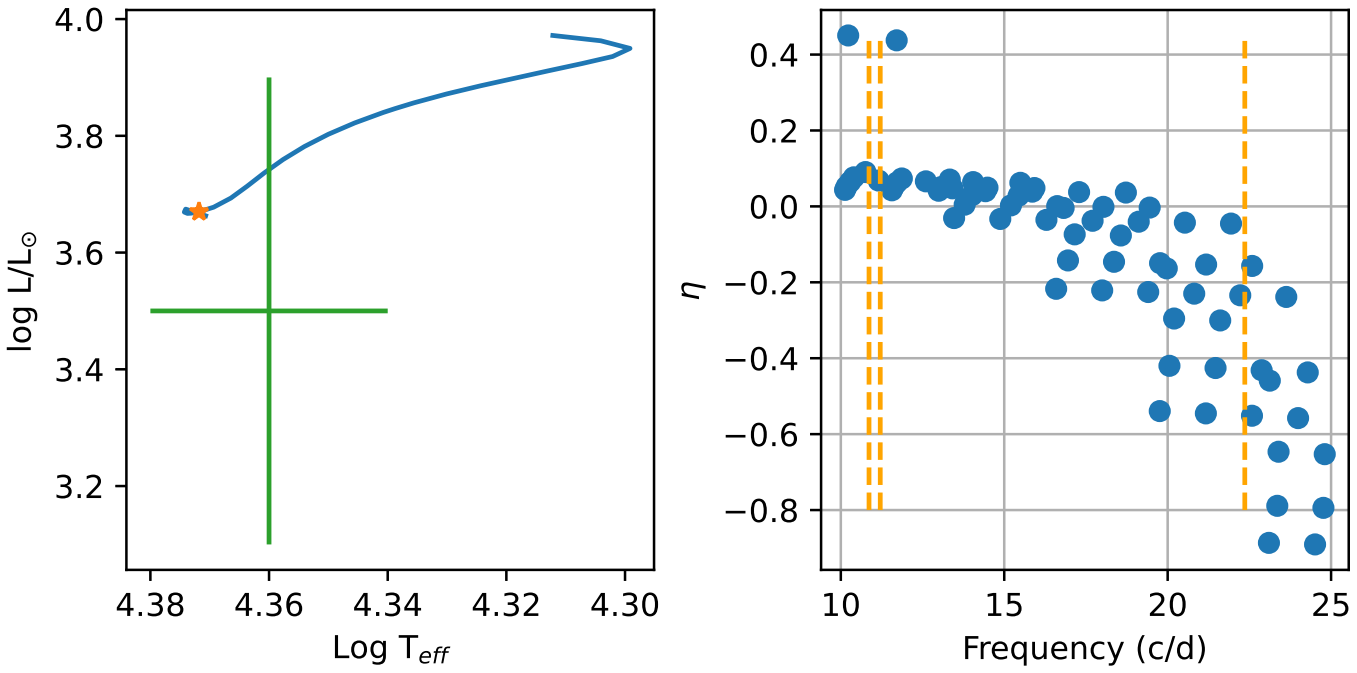

Figure 11. Same as Fig. 10 but for the primary star.

the error bar for the derived period of the phase variability. Further TESS observations of HD 156424 may improve this estimate.

Our derived variablity period for $f_{4,5}$ was in better agreement with previous data, with a period of 1490 ± 10 d. The phase variation in f_3 was poorly constrained, and our fit could also be consistent with a flat line. In all cases the errors on the phase calculations were large, and further monitoring of this system will be required to confirm and refine the period of the proposed third element.

We used the long-term phase variations to derive radial velocity curves, following the method outlined in Murphy et al. (2014). The resulting radial velocities for f_2 was around 155 m s^{-1}, while $f_{4,5}$ gave a much higher radial velocity of 8000 m s^{-1}, in better agreement with the literature values (Shultz et al. 2018). The radial velocities for f_3 are extremely small, with a maximum in our data set of 90 m s^{-1}. However, the variation is linear and we are likely underestimating the maximum radial velocity in the system. Using our new values for the periods and radial velocities results in a much smaller object as a third companion, with an upper limit of 0.05 M$_\odot$ derived from the f_2 fit. As this is an upper limit, the companion could well be a brown dwarf or a hot Jupiter.

Our asteroseismic models show the system is quite young, almost at the ZAMS, which is consistent with its membership in the Sco OB4 association. This is true across all metallicities we considered. Our best fitting model is an 9.8 $M_\odot$ model with Z = 0.02, a surface temperature of $\log T = 4.39$, a surface gravity of $\log g = 4.22$, and luminosity $\log L = 3.72$ (see Table 4, Case 1). The rotation velocity of this model is 146 km s^{-1}, which combined with the radius of 3.98 R$_\odot$ gives a rotation frequency of 0.725 d^{-1}, which is in good agreement with the observed rotation frequency f_1.

The A and B components of HD 156424 are within 1" on the sky, so we also considered the possibility that the pulsations originate in the lower mass secondary. However, we found no good fits to the observed frequency between 4 and 6 M$_\odot$. The mass of 5 M$_\odot$ is based on a luminosity difference of 2.3 mag in the y band (Tokovinin et al. 2010). However, the GAIA DR3 magnitudes, as well as the B and V magnitudes from the Tycho Double Star Catalogue (Fabricius et al. 2002) are much closer, and suggests the secondary has a mass of 8 M$_\odot$, more similar to the primary star.

This work was supported by an NSERC Discovery grant to CCL. V.K. acknowledges support from Mitacs, ACFAS, and is thankful to the Faculté des Études Supérieures et de la Recherch and to the Faculté des Sciences de l'Université de Moncton for financial support of this research. Computational resources for this project were provided by the Digital Research Alliance of Canada. TESS data was obtained from the MAST archive at doi:10.17909/T9RP4V. This work has made use of data from the European Space Agency (ESA) mission *Gaia* (https://www.cosmos.esa.int/gaia), processed by the *Gaia* Data Processing and Analysis Consortium (DPAC, https://www.cosmos.esa.int/web/gaia/dpac/consortium). Funding for the DPAC has been provided by national institutions, in particular the institutions participating in the *Gaia* Multilateral Agreement.

Software: astropy (Astropy Collaboration et al. 2013, 2018) MESA (Paxton et al. 2011, 2013, 2015, 2018, 2019), GYRE (Townsend & Teitler 2013; Townsend et al. 2018), lightkurve (Lightkurve Collaboration et al. 2018), Period04 (Lenz & Breger 2004)

REFERENCES

Alecian, E., Kochukhov, O., Petit, V., et al. 2014, A&A, 567, A28, doi: 10.1051/0004-6361/201323286

Astropy Collaboration, Robitaille, T. P., Tollerud, E. J., et al. 2013, A&A, 558, A33, doi: 10.1051/0004-6361/201322068

Astropy Collaboration, Price-Whelan, A. M., Sipőcz, B. M., et al. 2018, AJ, 156, 123, doi: 10.3847/1538-3881/aabc4f

Bell, K. 2022, Pyriod: Period detection and fitting routines, Astrophysics Source Code Library, record ascl:2207.007

Bigot, L., & Dziembowski, W. A. 2002, A&A, 391, 235, doi: 10.1051/0004-6361:20020824

Bigot, L., & Kurtz, D. W. 2011, A&A, 536, A73, doi: 10.1051/0004-6361/201116981

Blazère, A., Petit, P., Neiner, C., et al. 2020, MNRAS, 492, 5794, doi: 10.1093/mnras/stz3637

Buysschaert, B., Aerts, C., Bowman, D. M., et al. 2018, A&A, 616, A148, doi: 10.1051/0004-6361/201832642

Buysschaert, B., Neiner, C., Briquet, M., & Aerts, C. 2017, A&A, 605, A104, doi: 10.1051/0004-6361/201731012

Chojnowski, S. D., Hubrig, S., Labadie-Bartz, J., et al. 2022, Monthly Notices of the Royal Astronomical Society, 516, 2812, doi: 10.1093/mnras/stac2396

Deheuvels, S., Li, G., Ballot, J., & Lignières, F. 2023, Astronomy Astrophysics, 670, L16, doi: 10.1051/0004-6361/202245282

Fabricius, C., Høg, E., Makarov, V. V., et al. 2002, A&A, 384, 180, doi: 10.1051/0004-6361:20011822

Foreman-Mackey, D., Hogg, D. W., Lang, D., & Goodman, J. 2013, PASP, 125, 306, doi: 10.1086/670067

Gaia Collaboration, Prusti, T., de Bruijne, J. H. J., et al. 2016, A&A, 595, A1, doi: 10.1051/0004-6361/201629272

Gaia Collaboration, Vallenari, A., Brown, A. G. A., et al. 2023, A&A, 674, A1, doi: 10.1051/0004-6361/202243940

Goldstein, J., & Townsend, R. H. D. 2020, The Astrophysical Journal, 899

Hartkopf, W. I., Mason, B. D., Barry, D. J., et al. 1993, AJ, 106, 352, doi: 10.1086/116644

Jayaraman, R., Hubrig, S., Holdsworth, D. L., et al. 2022, The Astrophysical Journal Letters, 924, L10, doi: 10.3847/2041-8213/ac4333

Keszthelyi, Z., Meynet, G., Shultz, M. E., et al. 2020, Monthly Notices of the Royal Astronomical Society, 493, 518

Koposov, S., Speagle, J., Barbary, K., et al. 2022, joshspeagle/dynesty: v2.0.3, v2.0.3, Zenodo, doi: 10.5281/zenodo.7388523

Labadie-Bartz, J., Carciofi, A. C., Henrique de Amorim, T., et al. 2022, AJ, 163, 226, doi: 10.3847/1538-3881/ac5abd

Lecoanet, D., Bowman, D. M., & Van Reeth, T. 2022, MNRAS, 512, L16, doi: 10.1093/mnrasl/slac013

Lenz, P., & Breger, M. 2004, in IAU Symposium, Vol. 224, The A-Star Puzzle, ed. J. Zverko, J. Ziznovsky, S. J. Adelman, & W. W. Weiss, 786–790, doi: 10.1017/S1743921305009750

Li, G., Deheuvels, S., Ballot, J., & Lignières, F. 2022, Nature, 610, 43, doi: 10.1038/s41586-022-05176-0

Lightkurve Collaboration, Cardoso, J. V. d. M., Hedges, C., et al. 2018, Lightkurve: Kepler and TESS time series analysis in Python, Astrophysics Source Code Library. http://ascl.net/1812.013

Loi, S. T. 2020, Monthly Notices of the Royal Astronomical Society, 496, 3829, doi: 10.1093/mnras/staa1823

—. 2021, Monthly Notices of the Royal Astronomical Society, 504, 3711, doi: 10.1093/mnras/stab991

Mathis, S., & Bugnet, L. 2023, Astronomy Astrophysics, 676, L9, doi: 10.1051/0004-6361/202346832

Mathis, S., Bugnet, L., Prat, V., et al. 2021, Astronomy Astrophysics, 647, A112, doi: 10.1051/0004-6361/202039180

Murphy, S. J., Bedding, T. R., Shibahashi, H., Kurtz, D. W., & Kjeldsen, H. 2014, MNRAS, 441, 2515, doi: 10.1093/mnras/stu765

Neiner, C., Labadie-Bartz, J., Catala, C., et al. 2021, SF2A-2021: Proceedings of the Annual meeting of the French Society of Astronomy and Astrophysics, 161

Paxton, B., Bildsten, L., Dotter, A., et al. 2011, The Astrophysical Journal Supplement Series, 192, 35

Paxton, B., Cantiello, M., Arras, P., et al. 2013, The Astrophysical Journal Supplement Series, 208, 42

Paxton, B., Marchant, P., Schwab, J., et al. 2015, The Astrophysical Journal Supplement Series, 220, 44

Paxton, B., Schwab, J., Bauer, E. B., et al. 2018, The Astrophysical Journal Supplement Series, 234, 50

Paxton, B., Smolec, R., Schwab, J., et al. 2019, The Astrophysical Journal Supplement Series, 243, 44

Reese, D. R. 2022, Frontiers in Astronomy and Space Sciences, 9, 934579, doi: 10.3389/fspas.2022.934579

Rui, N. Z., Ong, J. M. J., & Mathis, S. 2023, Monthly Notices of the Royal Astronomical Society, 527, 6346, doi: 10.1093/mnras/stad3461

Shen, D., Li, G., Abdusamatjan, I., et al. 2023, The Astrophysical Journal, 955, doi: 10.3847/1538-4357/acf197

Shultz, M. E., Rivinius, T., Wade, G. A., et al. 2021, Monthly Notices of the Royal Astronomical Society, 504, 4850

Shultz, M. E., Wade, G. A., Rivinius, T., et al. 2018, MNRAS, 475, 5144, doi: 10.1093/mnras/sty103

Skilling, J. 2004, in American Institute of Physics Conference Series, Vol. 735, Bayesian Inference and Maximum Entropy Methods in Science and Engineering: 24th International Workshop on Bayesian Inference and Maximum Entropy Methods in Science and Engineering, ed. R. Fischer, R. Preuss, & U. V. Toussaint (AIP), 395–405, doi: 10.1063/1.1835238

Speagle, J. S. 2020, MNRAS, 493, 3132, doi: 10.1093/mnras/staa278

Stibbs, D. W. N. 1950, MNRAS, 110, 395, doi: 10.1093/mnras/110.4.395

Sun, M., Townsend, R. H. D., & Guo, Z. 2023, The Astrophysical Journal, 945, 11

Tokovinin, A., Mason, B. D., & Hartkopf, W. I. 2010, AJ, 139, 743, doi: 10.1088/0004-6256/139/2/743

Townsend, R. H. D., Goldstein, J., & Zweibel, E. G. 2018, Monthly Notices of the Royal Astronomical Society, 475, 879

Townsend, R. H. D., & Teitler, S. A. 2013, Monthly Notices of the Royal Astronomical Society, 435, 3406

VanderPlas, J. T. 2018, ApJS, 236, 16, doi: 10.3847/1538-4365/aab766